



# Evolution of the Postmerger Remnants from the Coalescence of Oxygen–Neon and Carbon–Oxygen White Dwarf Pairs

Chengyuan Wu<sup>1</sup> , Heran Xiong<sup>2</sup>, Jie Lin<sup>3</sup> , Yunlang Guo<sup>1,4</sup>, Xiaofeng Wang<sup>3</sup> , Zhanwen Han<sup>1</sup> , and Bo Wang<sup>1</sup> 

<sup>1</sup>Yunnan Observatories, Chinese Academy of Sciences, Kunming 650216, People's Republic of China; [wuchengyuan@ynao.ac.cn](mailto:wuchengyuan@ynao.ac.cn)

<sup>2</sup>Research School of Astronomy and Astrophysics, The Australian National University, Canberra, ACT 2611, Australia

<sup>3</sup>Physics Department and Tsinghua Center for Astrophysics, Tsinghua University, Beijing 100084, People's Republic of China

<sup>4</sup>University of Chinese Academy of Sciences, Beijing 100049, People's Republic of China

Received 2022 November 13; revised 2023 January 24; accepted 2023 January 27; published 2023 February 22

## Abstract

Although multidimensional simulations have investigated the processes of double white dwarf (WD) mergers, postmerger evolution only focused on the carbon–oxygen (CO) or helium (He) WD merger remnants. In this work, we investigate for the first time the evolution of the remnants stemming from the merger of oxygen–neon (ONe) WDs with CO WDs. Our simulation results indicate that the merger remnants can evolve to hydrogen- and helium-deficient giants with a maximum radius of about  $300 R_{\odot}$ . Our models show evidence that merger remnants more massive than  $1.95 M_{\odot}$  can ignite Ne before significant mass loss ensues, and they thus would become electron-capture supernovae. However, remnants with initial masses less than  $1.90 M_{\odot}$  will experience further core contraction and longer evolutionary time before reaching the conditions for Ne burning. Therefore, their fates are more dependent on mass-loss rates due to stellar winds and thus more uncertain. Relatively high mass-loss rates would cause such remnants to end their lives as ONe WDs. Our evolutionary models can naturally explain the observational properties of the double WD merger remnant IRAS 00500+6713 (J005311). As previously suggested in the literature, we propose and justify that J005311 may be the remnant from the coalescence of an ONe WD and a CO WD. We deduce that the final outcome of J005311 would be a massive ONe WD rather than a supernova explosion. Our investigations may be able to provide possible constraints on the wind mass-loss properties of the giants that have CO-dominant envelopes.

*Unified Astronomy Thesaurus concepts:* [White dwarf stars \(1799\)](#); [Stellar mergers \(2157\)](#)

## 1. Introduction

White dwarfs (WDs) are the most common evolutionary fate of single stars with initial masses lower than  $9\text{--}11 M_{\odot}$  (e.g., Nomoto & Kondo 1991; Ritossa et al. 1999; Eldridge & Tout 2004; Poelarends 2007; Siess 2007, 2010; Ibeling & Heger 2013; Doherty et al. 2017). It is estimated that there are about  $10^{10}$  WDs in our galaxy, of which  $2.5 \times 10^8$  reside in binaries consisting of two WDs (e.g., Nelemans et al. 2001; Holberg 2009; Napiwotzki 2009). About half of these binary WDs are close enough to begin mass transfer within a Hubble time.

The theoretical understanding of the evolution of WD merger remnants is based on using information from three-dimensional (3D) postmerger configurations to build one-dimensional (1D) models whose further evolution is computed in detail through their longer-duration phases. This procedure has been applied a number of times in the literature. For instance, Zhang et al. (2014) investigated the merger of carbon–oxygen (CO) and He WDs and found that the merger remnant can evolve to R CrB stars. Wu et al. (2022) investigated the postmerger evolution of massive CO WDs with He WDs and found that these systems contribute to a portion of ultramassive CO WDs. Brooks et al. (2017) investigated the merger of oxygen–neon (ONe) WDs with He WDs and found that these systems are related to electron-capture supernovae (ECSNe). Schwab et al. (2016) investigated

double CO WD mergers (see also Schwab 2021) and found that the corresponding super-Chandrasekhar-mass remnants can undergo iron core-collapse supernova (Fe-CCSN) explosions. However, no postmerger evolutionary model has been built so far to study ONe+CO WDs. For the evolutionary outcomes of such systems, although previous works suspected that they may be related to ECSNe, Type Ia supernovae, or neutron stars (NSs; e.g., Nomoto & Kondo 1991; Kitaura et al. 2006), detailed investigations are desperately needed.

In this work, based on the results of 3D simulations from Dan et al. (2014), we construct the 1D structures of ONe+CO WD merger remnants and investigate their evolution. We show that the final outcomes of such remnants are more complicated than previous deductions, which could be massive ONe WDs, ONeFe WDs, or NSs, depending on the mass of the merger remnant, the wind mass-loss process, and the effects of the treatment of convection. Besides, our model can perfectly explain the main observational properties of object J005311 (e.g., Gvaramadze et al. 2019; Oskinova et al. 2020; Lykou et al. 2023), which may provide a strong constraint on the wind mass-loss process of such merger remnants. The paper is organized as follows. In Section 2, we introduce our initial models of merger remnants. The evolution process of the remnants is shown in Section 3. The discussion of model uncertainties is given in Section 4. We analyze the final fate of J005311 in Section 5. The summary is given in Section 6.

## 2. Initial Models

Dan et al. (2014) performed a large set of WD merger simulations, including 225 pairs of double WD mergers. The



Original content from this work may be used under the terms of the [Creative Commons Attribution 4.0 licence](#). Any further distribution of this work must maintain attribution to the author(s) and the title of the work, journal citation and DOI.

mass range of ONe and CO WDs in their grid is from 1.10 to 1.20 and 0.65 to 1.05  $M_{\odot}$  spaced at mass intervals of 0.05  $M_{\odot}$ , respectively. Almost all of the mergers in their simulations are able to form stable remnants, except the double WD pairs with extremely low mass ratios (low-mass He WDs merge with ONe WDs), which do not show dynamical mass transfer during the merger. For the more massive merger remnant, Kashyap et al. (2018) simulated the process of a 1.20  $M_{\odot}$  ONe WD merger with a 1.10  $M_{\odot}$  CO WD and found that the merger yields a failed detonation that may produce a very faint and rapidly fading transient. In the present work, we only consider the postmerger evolution of stable merger remnants (i.e., Dan et al. 2014).

According to Dan et al. (2014), a double WD merger will form a remnant composed of a cool core, a hot envelope, a Keplerian disk, and a tidal tail from the inside out. Based on the results of 3D simulations, they provided 1D remnant structure profiles, including key information on the merger remnants, such as their maximum temperature ( $T_{\max}$ ), the density at the location of the maximum temperature ( $\rho_{\max}$ ), their core mass ( $M_{\text{core}}$ ), their envelope mass ( $M_{\text{env}}$ ), and their disk mass ( $M_{\text{disk}}$ ), among others. By considering the structures of merger remnants from Dan et al. (2014), Schwab et al. (2016) developed the energy-injecting prescription to map the initial configurations of the remnants and investigated the evolution of double CO WD mergers (see also Schwab 2021).

In this work, we use a prescription similar to the one described in Schwab et al. (2016) to construct a series of ONe+CO WD merger remnants with ONe WD mass in the range from 1.1 to 1.2  $M_{\odot}$  and total mass from 1.60 to 2.25  $M_{\odot}$  spaced at mass intervals of 0.05  $M_{\odot}$  as our fiducial models by employing the stellar evolutionary code MESA (version 12778; e.g., Paxton et al. 2011, 2013, 2015, 2018, 2019). In addition, we also constructed double CO WD merger remnants to compare with the observations (detailed information can be found in Section 5). Since the mass of the tidal tail only occupies a significantly small portion of the total mass of the remnants, we ignore the influence of the tidal tail and construct the merger remnants consisting only of a core, an envelope, and a disk. As proved by Schwab (2021), this approach has an almost negligible influence on the initial profile of the remnants.

The detailed prescriptions for constructing the initial models are presented as follows. First, we create a series of pre-main-sequence stars with masses equal to the total masses of the merger remnants and evolve these models with nuclear reactions and elemental mixing turned off until the central density reaches  $10^3 \text{ g cm}^{-3}$ . Second, we resume the evolution, using the built-in capability of MESA to relax our model to a specified composition. In Dan et al. (2014), the composition of ONe WDs includes 60%  $^{16}\text{O}$ , 35%  $^{20}\text{Ne}$ , and 5%  $^{24}\text{Mg}$ , and CO WDs include 40%  $^{12}\text{C}$  and 60%  $^{16}\text{O}$ . Thus, the merger remnants in our models consist of an ONe core and an outer CO envelope. Once the composition relaxation is achieved, we evolve these models until their central densities reach  $10^5 \text{ g cm}^{-3}$ .

In order to construct the thermal structures of the merger remnants, we inject energy into different mass zones to alter the temperature and density until they reach target profiles, i.e., an isothermal core with a temperature of  $10^8 \text{ K}$ , surrounded by a hot envelope and a disk. The target profiles are as follows.

For  $0 \leq M_r \leq M_{\text{core}}$ ,

$$T(M_r) = T_{\text{core}}. \quad (1)$$

For  $M_{\text{core}} \leq M_r \leq M_{\text{core}} + M_{\text{env}}$ ,

$$s(M_r) = s_{\text{core}} + [s_{\text{env}} - s(M_{\text{core}})] \frac{M_r - M_{\text{core}}}{M_{\text{peak}}}. \quad (2)$$

And for  $M_{\text{core}} + M_{\text{env}} \leq M_r \leq M_{\text{tot}}$ ,

$$s(M_r) = s_{\text{env}}. \quad (3)$$

In the equations,  $M_{\text{core}}$ ,  $M_{\text{env}}$ , and  $M_{\text{peak}}$  are, respectively, core masses, envelope masses, and the mass coordinates of the maximum temperature of the merger remnants, which are related to the total masses of the remnants ( $M_{\text{tot}}$ ) and the mass ratios of the double WDs before the mergers ( $q$ ), i.e.,

$$M_{\text{core}} = M_{\text{tot}}(0.7786 - 0.5114q), \quad (4)$$

$$M_{\text{env}} = M_{\text{tot}}(0.2779 - 0.464q + 0.716q^2), \quad (5)$$

$$M_{\text{peak}} = M_{\text{tot}}(0.863 - 0.3335q). \quad (6)$$

In Equation (1),  $T_{\text{core}} = 10^8 \text{ K}$  is the typical temperature of the massive WD used in our simulations. The  $M_{\text{peak}}$  in Equation (2) represents the mass coordinate at the highest temperature. The  $s_{\text{core}}$  and  $s_{\text{env}}$  in Equations (2) and (3) are, respectively, the specific entropies of the core and the envelope. We set  $s_{\text{core}}$  to be the specific entropy of the core when  $T_{\text{core}} = 10^8 \text{ K}$ , and  $s_{\text{env}}$  is equal to the following equation:

$$\log(s_{\text{env}}/\text{erg g}^{-1} \text{K}^{-1}) = 8.7 + 0.3(M_{\text{tot}}/M_{\odot} - 1.5). \quad (7)$$

We use a very short time step (in seconds) to complete the energy injection process to guarantee the corresponding process cannot change the target profile (for more details of the method, see Schwab et al. 2016 and Schwab 2021).

After the energy injection process, we obtained the initial structures of the merger remnants. Figure 1 shows the temperature–mass coordinate ( $T$ – $M_r$ ) and temperature–density ( $T$ – $\rho$ ) profiles of different merger remnants after the energy injection processes. Our initial remnant models have isothermal cores at  $10^8 \text{ K}$ . The  $M_{\text{env}}$  and  $T_{\max}$  of the merger remnants increase with the increasing mass ratio of the progenitor double WDs and their total masses, which is consistent with 3D simulations.

The comparison of some major parameters of our models with 3D simulations are presented in Figure 2. Although  $T_{\max}$  and the mass coordinate are slightly different with 3D simulations, our models conform to the variation trend of different merger remnants. Note, however, that the subsequent evolution of the remnants may be sensitive to the structures of the initial models. We analyze the influence of the initial conditions on the evolution of merger remnants in Section 4.1.

### 3. Evolution of the Remnant of ONe+CO WD Mergers

#### 3.1. Input Physics

Since the outer layers of such merger remnants consist of carbon and oxygen, we use an OPAL type 2 opacity table to calculate the evolution of the remnants (e.g., Iglesias & Rogers 1996). When the remnants evolve to the giant phase, the surface temperature may decrease to about  $\log(T/\text{K}) = 3.65$ . Since the lower boundary of the OPAL tabulations is  $\log(T/\text{K}) = 3.75$ , as in Schwab et al. (2016), we

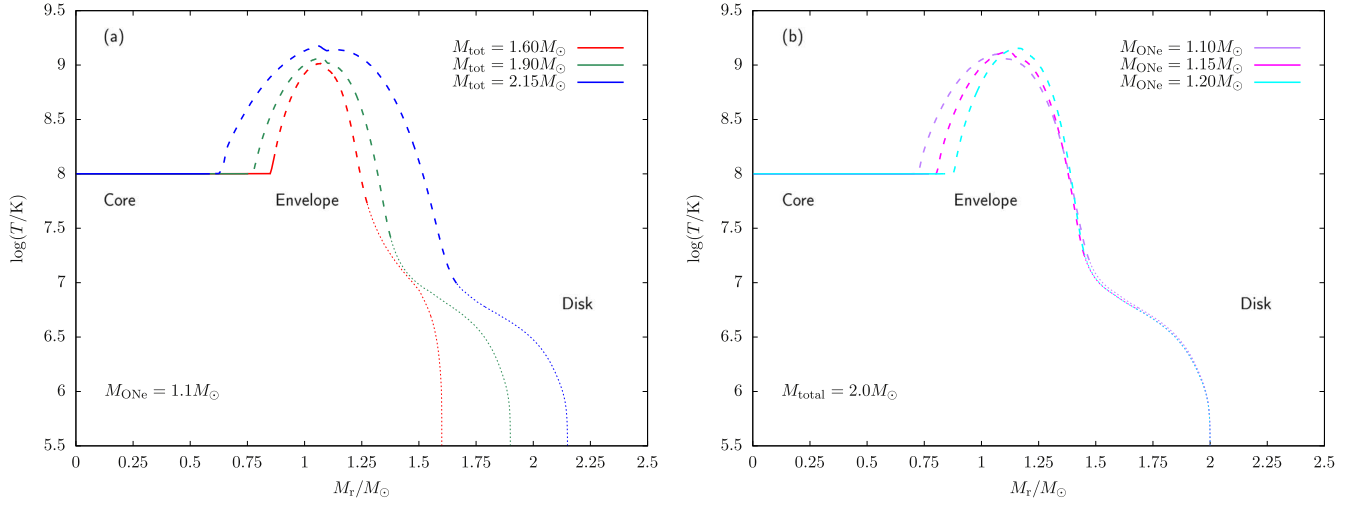


**Figure 1.** Temperature–mass coordinate profile of the merger remnants just after the energy injection processes. Panel (a): temperature profiles of three merger remnants of different total masses and the same ONe WD mass. Panel (b): temperature profiles of three merger remnants of equal ONe WD mass and different total masses. Different lines in panel (a) and (b) represent the corresponding structures of double WD mergers with various mass ratios.

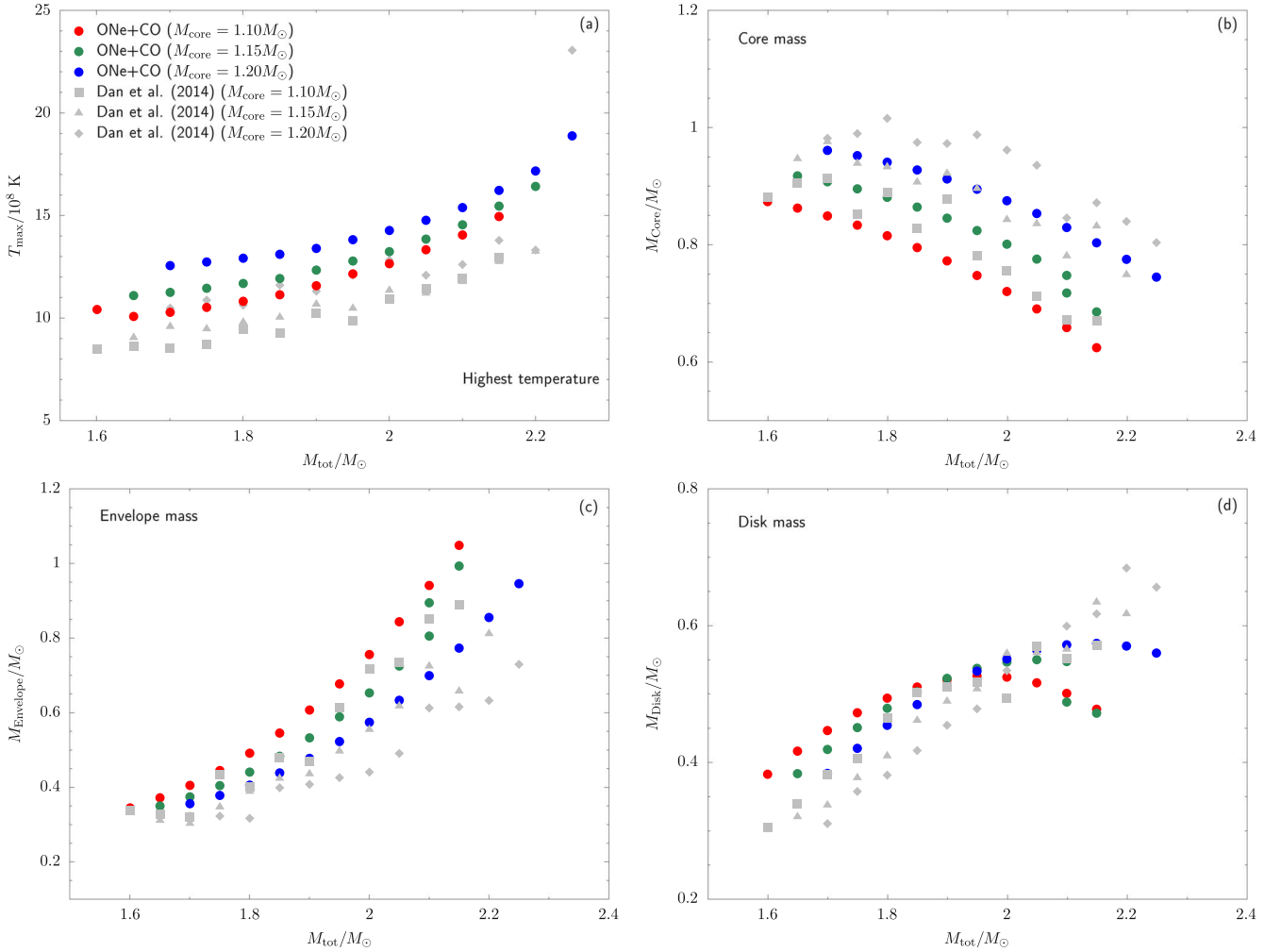


**Figure 2.** Main properties of the merger remnants ( $T_{\max}$  in panel (a), core mass in panel (b), envelope mass in panel (c), and disk mass in panel (d)) with different initial ONe and CO WD masses. Red, green, and blue filled circles in each panel represent the parameters of the merger remnants with initial ONe WD masses equal to 1.10, 1.15, and  $1.20 M_{\odot}$  in our models, whereas gray diamonds in each panel represent the corresponding parameters resulting from Dan et al. (2014).

adopt the Kasen opacities to deal with the low-temperature conditions and blend the OPAL and Kasen opacities between  $\log(T/K) = 4.1$  and  $4.2$ . This supplement is suitable for H- and He-deficient cool giant-like stars.

The nuclear reaction network used in the present work is “wd\_aic.net,” which includes “co\_burn.net” in “MESA default,” and we artificially added four isotopes (i.e.,  $^{20}\text{O}$ ,  $^{20}\text{F}$ ,  $^{24}\text{Ne}$ , and  $^{20}\text{Na}$ ) and the corresponding weak reactions in order to calculate the electron-capture process. The weak interaction rates are from Schwab et al. (2015). We apply “MESA default” screening factors to correct nuclear reaction rates for plasma interactions (e.g., Chugunov et al. 2007). The cooling rates from thermal neutrinos are derived from the fitting formulae of Itoh et al. (1996).

As the remnant expands toward the giant phase, the superadiabatic gradient arising in radiation-dominated envelopes can force the adoption of prohibitively short time steps. To circumvent this issue, we apply the treatment of convective energy transport “MLT++” (e.g., Paxton et al. 2013) to reduce the superadiabaticity in the radiation-dominated convective regions. As soon as Ne burning is ignited under the CO envelope, the inwardly propagating flame will leave a thin burning shell with an extremely high-energy release rate. Previous works found that the treatment of convection can affect the evolution of the stars; for example, a small amount of convective boundary mixing can remove the physical conditions required for the off-center burning flame in super-AGB stars (e.g., Denissenkov et al. 2013; Jones et al. 2014; Farmer et al. 2015; Jones et al. 2016a). In the present work, we consider an overshooting process with parameters of  $f = 0.014$  and  $f_0 = 0.004$  to calculate the inwardly propagating Ne flame (e.g., Denissenkov et al. 2013; Wu et al. 2020). We constrain the time resolution in our calculations by adopting “varcontral = 3d - 4.” When the increasing central density of the remnant reaches  $\approx 10^{9.5} \text{ g cm}^{-3}$ , we constrain the time step by controlling the change of the central density ( $\text{delta\_lgRho\_cntr\_limit} = 1\text{d} - 3$ ) to guarantee precision in simulating the electron-capture process. In order to have a better treatment of the propagation of the off-center flame, we control the spatial resolution by changing “dlog\_burn\_c\_dlogP\_extra = 0.1” and “dlog\_burn\_ne\_dlogP\_extra = 0.1” to increase the mesh grid around the flame.

Some physical mechanisms have not been included in our fiducial models, such as the wind mass-loss process, Urca-process cooling, stellar rotation, etc. We will discuss the effects of the corresponding uncertainties in Section 4.

### 3.2. Postmerger Evolution

After constructing the initial models of the merger remnants, we restored the nuclear reactions and mixing process to let the remnants evolve forward in time. The detailed physical inputs of our fiducial models can be found in the Appendix. The evolutionary features of two representative examples (a  $1.1 M_{\odot}$  ONe WD merges with a  $0.8 M_{\odot}$  CO WD,  $M_{\text{tot}} = 1.90 M_{\odot}$ ; a  $1.1 M_{\odot}$  ONe WD merges with a  $0.85 M_{\odot}$  CO WD,  $M_{\text{tot}} = 1.95 M_{\odot}$ ) are presented in Figure 3. Owing to the initially compact configurations, the remnants experience an extremely short thermal adjustment stage (8 hr) prior to the ignition of carbon. Carbon burning starts below the convective envelope (the CO envelope is partially convective because of the energy injection process), proceeds through thermal pulses, and forces the

formation of an inner convective zone due to the high-energy release. Nuclear energy is then transformed into the work of expansion on the envelope, resulting in the increase of the radius and opacity. As the temperature gradient increases, the convective zone gradually develops in the CO envelope. After the remnants approach the giant phase, carbon burning proceeds steadily on the bottom of the shell, resulting in the mass increase of the ONe core. During the giant phase, the remnants can expand to about  $300 R_{\odot}$  in tens of years after the merger. This giant stage is the longest part of the evolution between the merger and the end of our calculations.

Carbon burning becomes stationary after some thermal pulses. The steady carbon burning leads to the mass increase of the degenerate core. The evolution of such a giant-like object complies with the core mass–luminosity relation (e.g., Jeffery 1988). The major difference between the  $1.90$  and  $1.95 M_{\odot}$  cases lies in the time when the Ne ignition occurs.

For the less massive remnants, carbon burning cannot trigger the Ne ignition immediately after the merger, and the remnants’ cores need to experience longer evolutionary times to increase in mass. In this case, the ignition of Ne occurs after the electron-capture process of  $^{24}\text{Mg}$  (i.e., 3015 yr after merger), when the temperature and density of the Ne-burning region reach  $\log(T/K) = 9.11$  and  $\log(\rho/\text{g cm}^{-3}) = 7.23$ , respectively. The mass coordinate of Ne ignition is at  $M_r = 1.368 M_{\odot}$ , just below the carbon-burning shell ( $M_r = 1.388 M_{\odot}$ , which corresponds to the mass of the Ne core).

For the massive case, Ne ignition occurs 209 yr after the merger, at  $M_r = 1.186 M_{\odot}$  (relatively far away from the carbon-burning shell, located at  $M_r = 1.360 M_{\odot}$ ), when the temperature and density of the Ne-burning region reach  $\log(T/K) = 9.23$  and  $\log(\rho/\text{g cm}^{-3}) = 7.37$ , respectively. This means that the massive remnant does not experience a significantly long core increase phase, which leads to shorter evolutionary times of the remnants.

The major difference between these two cases can also be reviewed from the elemental abundance distributions (panels (c) and (d) of Figure 3). Because the position of Ne ignition is very close to the CO-burning shell in the  $1.90 M_{\odot}$  case, the convective region caused by Ne burning penetrates into the CO envelope, resulting in the dredge-up of ONe-rich material out to the envelope. The abundance of Ne in the CO envelope can reach about 30%. Meanwhile, note that the thickness of the Si mantle is equal to the width of the convective region caused by the Ne burning; therefore, the Si mantles in two cases are different because of the different positions of the Ne ignitions.

In addition to the abovementioned evolutionary times, the final densities of the two cases considered also show differences. To better analyze these differences, we present the Hertzsprung–Russell diagram (HRD) and central density–temperature profiles for a series of remnants in Figure 4. Although the evolutionary processes follow similar trends on the HRD, they show differences in the  $T_c$ – $\rho_c$  profile. Due to the different ignition times of Ne mentioned above, the corresponding two classes of remnants ( $M \leq 1.90$  and  $\geq 1.95 M_{\odot}$ ) can evolve to different central densities when the explosion occurs. Previous multidimensional dynamical simulations of supernova explosions suggested that for the pure ONe core, Ne or O explosions occurring at a higher central density ( $\log(\rho_c/\text{g cm}^{-3}) > 9.97$ ) will result in the formation of an NS, whereas for the cases in which Ne or O explosions occur at a lower central density ( $\log(\rho_c/\text{g cm}^{-3}) < 9.97$ ), an ONeFe

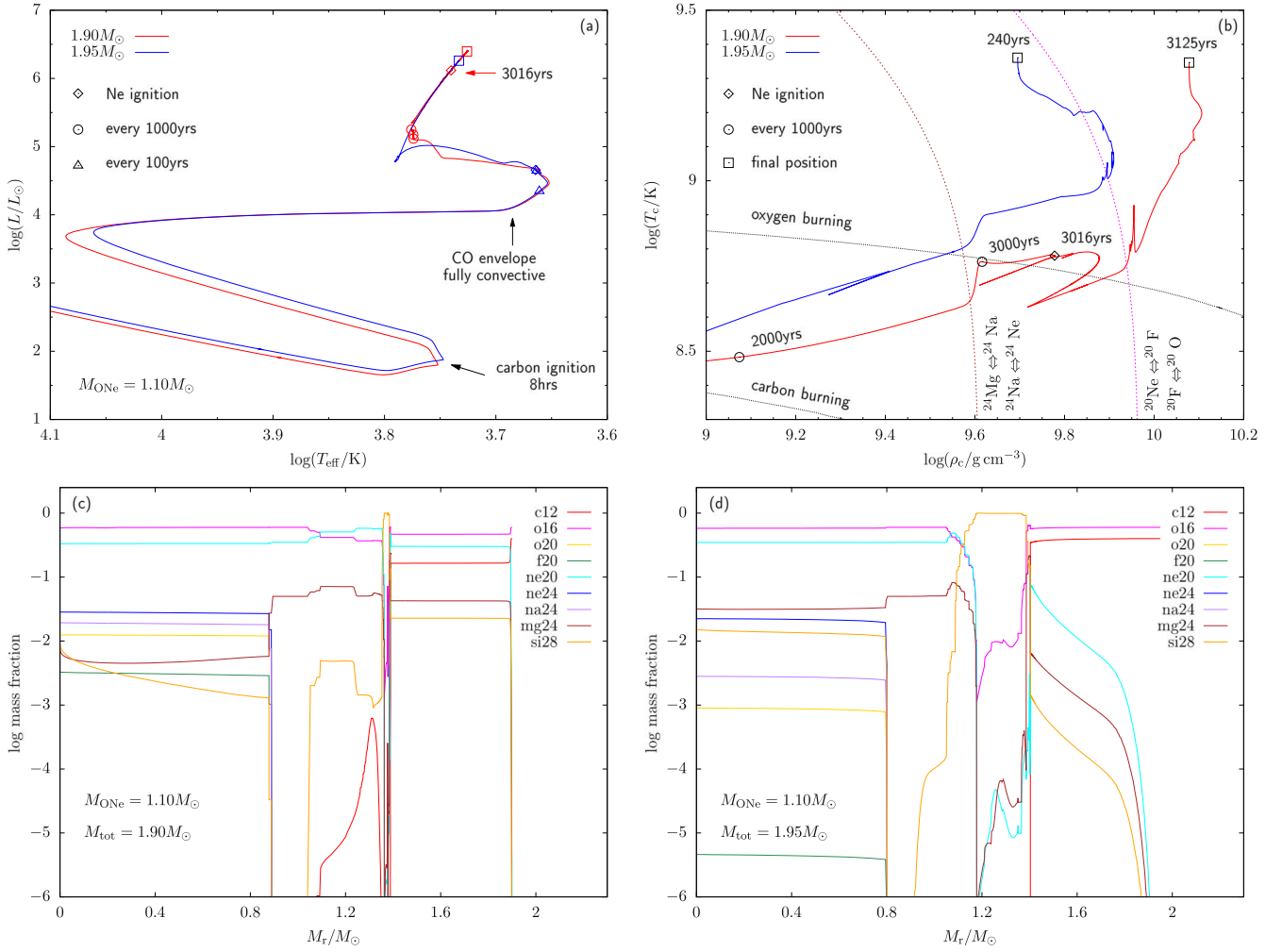


**Figure 3.** Example of the evolution of two merger remnants (a  $1.1 M_{\odot}$  ONe WD merges with a  $0.8 M_{\odot}$  CO WD,  $M_{\text{tot}} = 1.90 M_{\odot}$ ; a  $1.1 M_{\odot}$  ONe WD merges with a  $0.85 M_{\odot}$  CO WD,  $M_{\text{tot}} = 1.95 M_{\odot}$ ). Panel (a): HRD. Panel (b): central density–temperature evolution. Panels (c) and (d): elemental abundance distributions of  $1.90$  and  $1.95 M_{\odot}$  merger remnants at the final stage of their evolution just prior to the explosions. In panels (a) and (b), diamonds represent the position of Ne ignition, whereas circles and triangles represent every 1000 and 100 yr after merger, respectively. Squares in panel (b) represent the position of the final evolutionary stage, near which the corresponding evolutionary times are labeled. Black dotted lines in panel (b) represent the carbon- and oxygen-burning lines, whereas brown and magenta dotted lines represent the starting lines of the electron-capture reactions of  $^{24}\text{Mg}$  and  $^{20}\text{Ne}$ . Note that the diamond on the blue line of panel (b) is out of range.

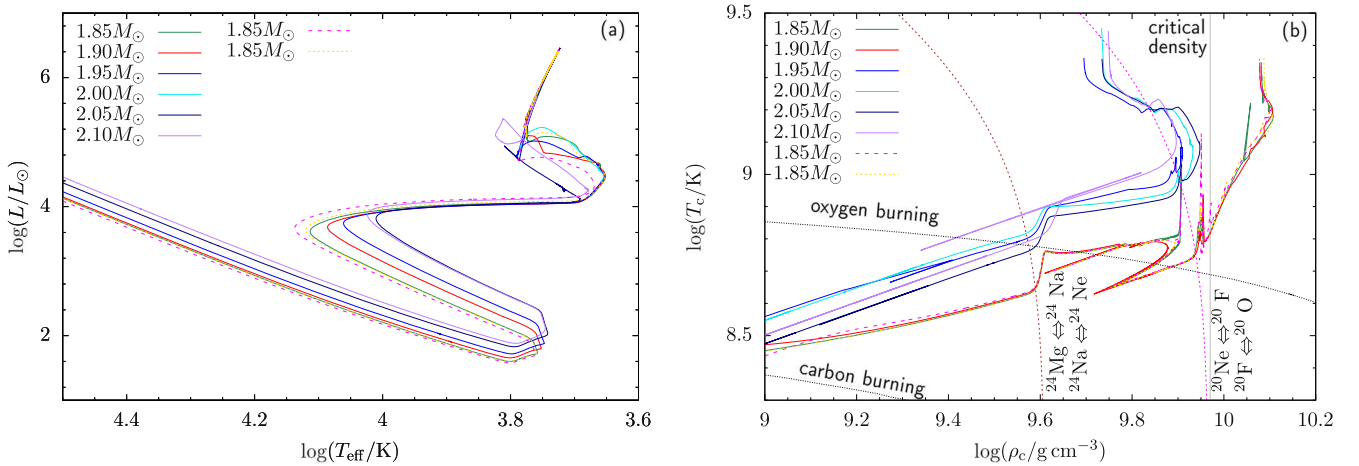


**Figure 4.** Evolutionary tracks of different remnants ( $M_{\text{ONe}}^1 = 1.10 M_{\odot}$ ) in the HRD and central temperature–density profile. Black dotted lines in panel (b) represent the carbon- and oxygen-burning conditions, whereas brown and magenta dotted lines represent the starting lines of the electron-capture reactions of  $^{24}\text{Mg}$  and  $^{20}\text{Ne}$ . The gray vertical line in panel (b) represents the critical density, below which the explosion of the core will lead to the formation of an ONeFe WD and above which will lead to the formation of an NS.

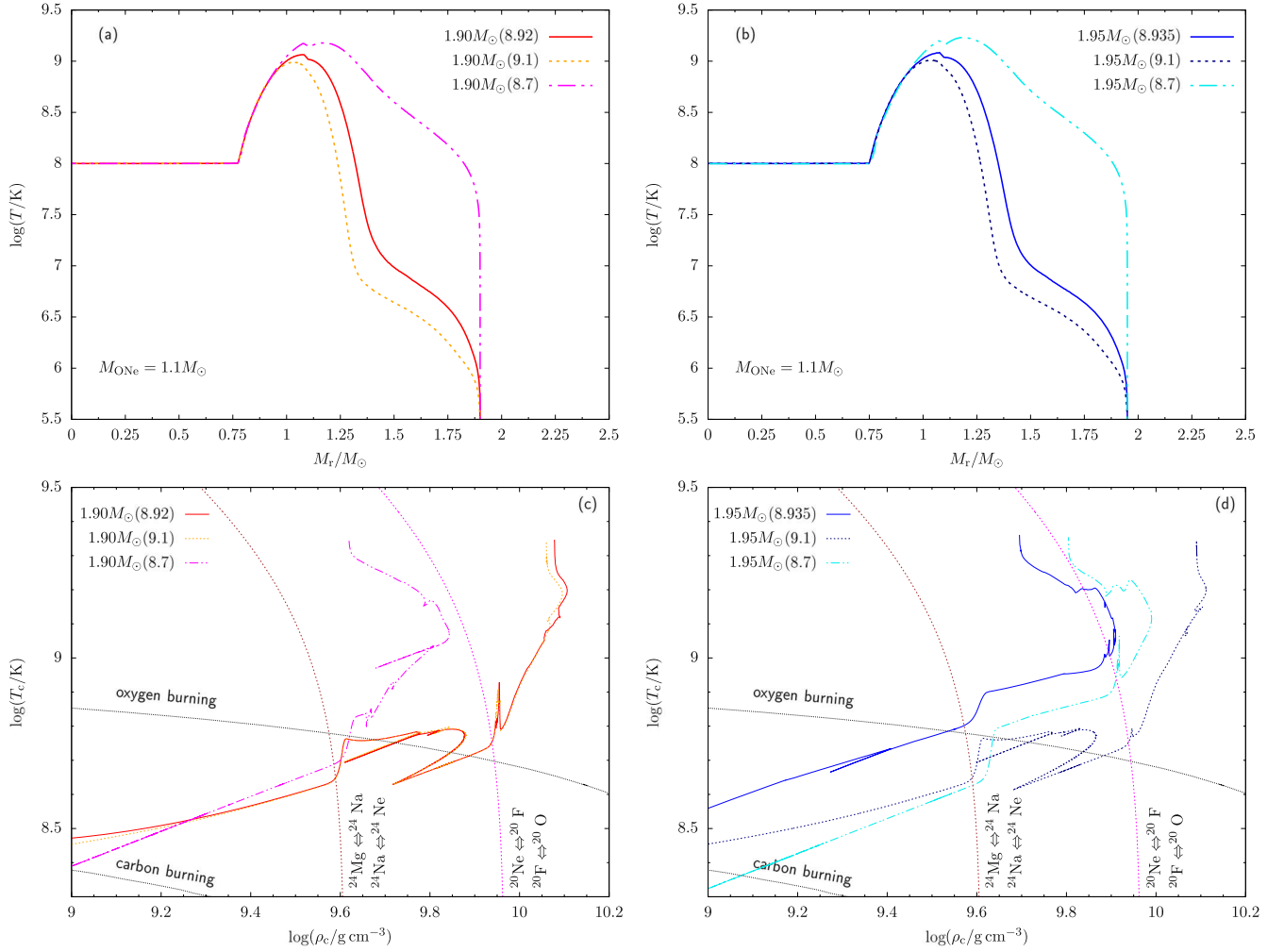


**Figure 5.** Initial profiles and evolutionary tracks of 1.90 and 1.95  $M_{\odot}$  merger remnants with different envelope entropies. Panels (a) and (b): initial  $T$ - $M$  profiles. The red (blue) solid line represents our fiducial model, whereas the magenta (cyan) double dotted-dashed and gold (navy) dotted lines represent remnants with lower ( $\ln(s_{\text{env}}/\text{erg g}^{-1} \text{K}^{-1}) = 8.7$ ) and higher ( $\ln(s_{\text{env}}/\text{erg g}^{-1} \text{K}^{-1}) = 9.1$ ) envelope entropies, respectively. Panels (c) and (d): evolutionary tracks of merger remnants in the  $\log T_c - \log \rho_c$  diagram.

core will be left behind after the explosion (e.g., Jones et al. 2016b, 2019). Our results indicate that the final outcomes of double WD mergers strongly depend on the initial remnant masses.

#### 4. Model Uncertainties

Previous studies indicate that some pivotal physical mechanisms such as the wind mass-loss process can significantly affect the evolution of double WD merger remnants (e.g., Schwab 2019; Schwab 2021; Wu et al. 2022). We discuss the influence of these mechanisms in this section.

##### 4.1. Initial Structure

The initial structures of the merger remnants of our models result from the fitting formulae in Dan et al. (2014). The comparisons of some major parameters of our models with those from 3D simulations are presented in Figure 5. Although  $T_{\text{max}}$  and the mass coordinate are slightly different from the 3D simulations, our models conform to the variation trend of different merger remnants. However, the fitting formulae for the different properties of the merger remnants in Dan et al. (2014) can only explain 75%–90% of the variance. In order to investigate the

effects of initial model uncertainties, we constructed models with different  $T_{\text{max}}$  by changing the entropy of the envelope ( $s_{\text{env}}$  in Equation (7)). Basically, a higher envelope entropy can lead to a lower  $T_{\text{max}}$  because of the decreased density of the envelope. On the contrary, a lower envelope entropy can result in a higher  $T_{\text{max}}$ . Detailed physical inputs are given in the Appendix

The evolution of 1.90 and 1.95  $M_{\odot}$  merger remnants with different initial  $T_{\text{max}}$  are shown in Figure 5. Decreasing the envelope entropy (increasing  $T_{\text{max}}$ ) in our models shifts the lower mass threshold for the formation of a ONeFe WD downward. For the less massive remnant ( $M = 1.90 M_{\odot}$ ), increasing the envelope entropy (a lower  $T_{\text{max}}$ ) has no influence on the final outcome, whereas increasing  $T_{\text{max}}$  will lead to a similar evolutionary track as the massive remnant. On the other hand, the outcome of our 1.95  $M_{\odot}$  model is not affected by an increase in  $T_{\text{max}}$  but delays Ne ignition if  $T_{\text{max}}$  is decreased. The dependence of the outcomes with  $T_{\text{max}}$  reflects the influence of the initial remnant mass on the final fate of the considered models.

##### 4.2. Mass-loss Rate

The wind mass-loss prescription has not been considered in our fiducial models. During their evolution, the merger remnants can evolve to the giant phase and produce dusty

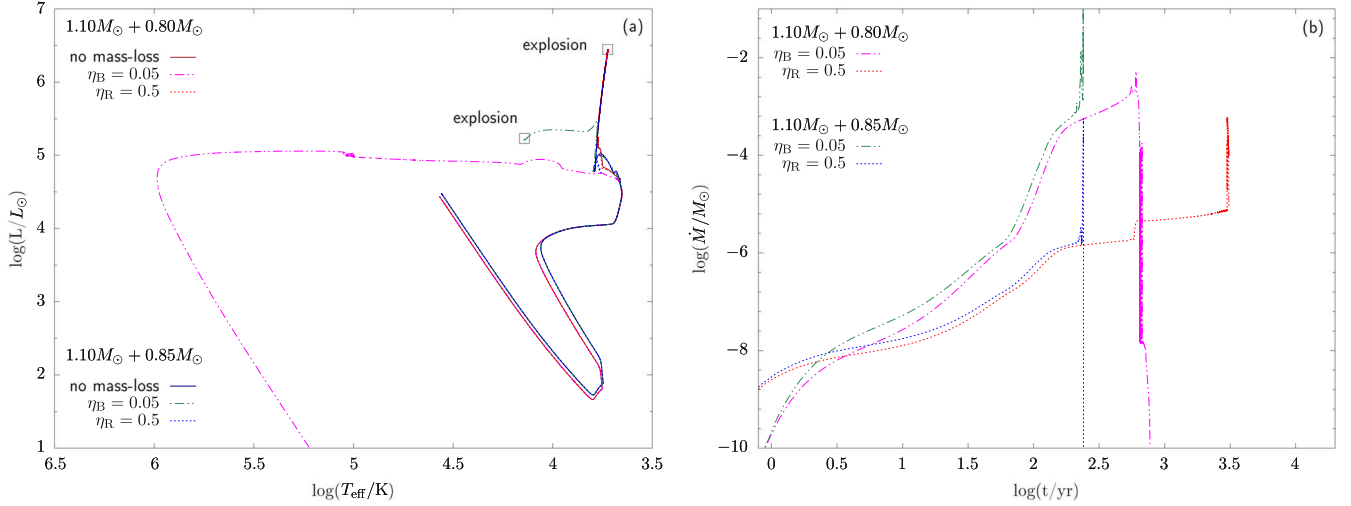


**Figure 6.** Evolution of 1.90 and 1.95  $M_{\odot}$  ONe+CO WD merger remnants under different wind mass-loss prescriptions. Panel (a): HRD. The representatives of each line are labeled. Squares on each line represent the positions on the HRD of the corresponding models when supernova explosions occur. Panel (b): evolution of mass-loss rate.

winds, which may have an influence on their evolution. However, the physics of the winds of such H-/He-deficient giants is not well understood, and mass-loss rates cannot be constrained from the observation so far. In the present work, we simply explore the effect of mass loss by considering Reimers' (e.g., Reimers 1975) and Bloeker's (e.g., Bloeker 1995) wind mass-loss prescription with "MESA default" values of wind coefficients ( $\eta_R = 0.5$ ;  $\eta_B = 0.05$ ). Detailed physical inputs are given in the Appendix.

Figure 6 presents the evolutionary tracks of 1.90 ( $1.10 + 0.80$ ) and 1.95 ( $1.10 + 0.85$ )  $M_{\odot}$  ONe+CO WD merger remnants under Reimers' and Bloeker's wind mass-loss prescriptions. During the giant phase, the wind mass-loss rate with Reimers' wind prescription is significantly less than that under Bloeker's wind prescription, which only exceeds the order of magnitude of  $10^{-4} M_{\odot} \text{ yr}^{-1}$  at the end of the evolution. This means that Reimers' wind cannot significantly change the total masses of the remnants, and the final outcome of the remnants is the same as those without wind mass loss. However, under Bloeker's wind prescription, the remnants can maintain a high mass-loss rate during the whole giant phase, which effectively decrease the total mass of the remnants. For the less massive remnants ( $M \leq 1.90 M_{\odot}$ ), all of the CO envelope can be lost during the evolution, resulting in the formation of ONe WDs. Although the strong wind mass-loss process can obviously affect the massive remnants ( $M \geq 1.95 M_{\odot}$ ), because of the short evolutionary time, the final mass of the initially massive models can still be high enough to trigger the electron-capture reactions that lead to the formation of ONeFe WDs. Our results indicate that wind prescriptions play a critical role in investigating the evolution of double WD merger remnants. Whether NSs can be formed through ONe+CO WD binary systems may strongly depend on the wind efficiency after the merger.

#### 4.3. Initial Helium Abundance

According to the stellar evolutionary results, there is a thin He shell outside the CO core for the low-mass CO WDs. The 0.5–0.6  $M_{\odot}$  CO WDs in the Dan et al. (2014) models have 0.1  $M_{\odot}$  of He envelope. During the merger process, He is fully mixed with CO material and forms the hot envelope

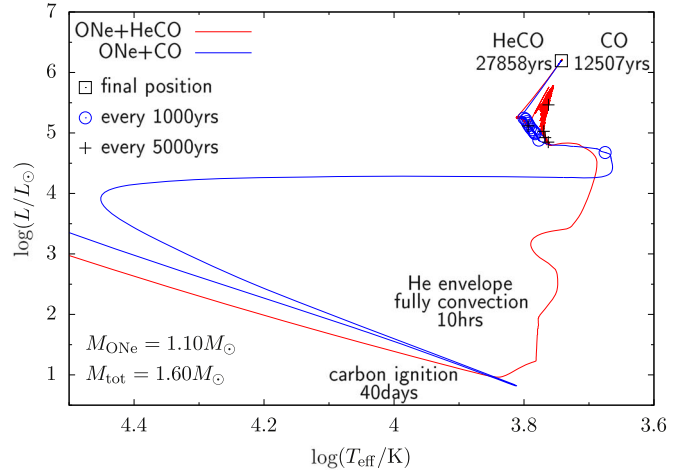


**Figure 7.** Evolutionary tracks of 1.60  $M_{\odot}$  ONe+CO and ONe+HeCO WD merger remnants on the HRD. Black plus signs on the red curve represent every 5000 yr during evolution, whereas blue circles on the blue curve represent every 1000 yr during evolution. The black square represents the final position on the HRD for each evolutionary track.

surrounding the postmerger ONe WD. The exist of He in the merger remnant may influence the evolution of the remnants. To investigate the effect of the existence of He in our initial models, we build an alternative 1.60  $M_{\odot}$  ONe+CO WD merger remnant by changing the composition described in Section 2 to 40%  $^{12}\text{C}$ , 40%  $^{16}\text{O}$ , and 20%  $^4\text{He}$ . Then, we let this model evolve in time. Detailed physical inputs are given in the Appendix.

In Figure 7, we present the evolutionary tracks of 1.60  $M_{\odot}$  ONe+CO (original composition) and ONe+HeCO (alternative composition) WD merger remnants on the HRD. Due to the nonnegligible amount of He in the envelope, the temperature required for the He-rich envelope burning is expected to be lower than that without helium. Thus, the convective envelope develops very fast in the He-rich envelope; it becomes fully convective only 10 hr after merger, resulting in the difference during the luminosity increase phase. Furthermore, owing to the lower nuclear reaction rate in the He-rich burning shell

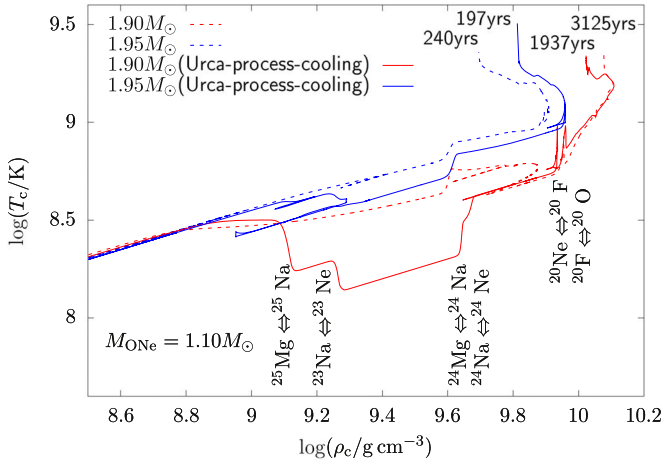


**Figure 8.** Evolutionary tracks of 1.90 and 1.95  $M_{\odot}$  merger remnants in a  $\log T_c$ – $\log \rho_c$  diagram. Solid and dashed lines represent the corresponding tracks with and without considering Urca-process cooling during evolution, respectively.

compared with the pure CO counterpart, the ONe+HeCO WD merger remnants need a longer evolutionary time to increase the core mass until explosive Ne/O ignition occurs. Although the existence of He in the envelope influences the evolutionary time of the remnants, the final outcome is the same.

#### 4.4. Urca-process Cooling

Urca-process cooling may affect the central temperature during the evolution. We construct 1.90 and 1.95  $M_{\odot}$  merger remnants with 5%  $^{23}\text{Na}$  and 1%  $^{25}\text{Mg}$  in the initial ONe WD (e.g., Schwab et al. 2017) and simulate their evolution to investigate the effect of Urca-process cooling. Detailed physical inputs are given in the Appendix.

From Figure 8, we can see that by considering Urca-process cooling, the central temperature decreased during the stage of the electron-capture reaction of  $^{25}\text{Mg}$  and  $^{23}\text{Na}$ , which is similar to what happened in the mass-accretion WD systems (e.g., Schwab et al. 2017). The remnants evolve faster when Urca-process cooling is considered. This is because, due to the electron capture of  $^{25}\text{Mg}$  and  $^{23}\text{Na}$ , the central temperature of the remnant decreases, resulting in the shrinking of the ONe core, which promotes the occurrence of the electron-capture reaction of  $^{24}\text{Mg}$  and  $^{20}\text{Ne}$ . The examples show that the final fates of the merger remnants do not change when considering Urca-process cooling, which means that the corresponding effect is a minor factor in such merger remnants.

#### 4.5. Rotation

During the merger process, a portion of the orbital angular momentum could be left in the remnant. Rotation can decrease the density in the burning zone and enhance the mixing process, which may have an influence on the evolution of the remnants.

In order to investigate the rotational effects, we inject torque into different mass zones in the 1.90 and 1.95  $M_{\odot}$  initial models. The 3D simulations predicted that the merger remnant consists of a corotating core with  $\Omega_c \approx 0.23$ – $0.52 \text{ rad s}^{-1}$  (depending on the total mass and mass ratio) and a differential rotating envelope in which  $\Omega_e$  gradually decreases from the inside out. In the present work, we consider two different rotational velocities. The fast rotational models have a uniform

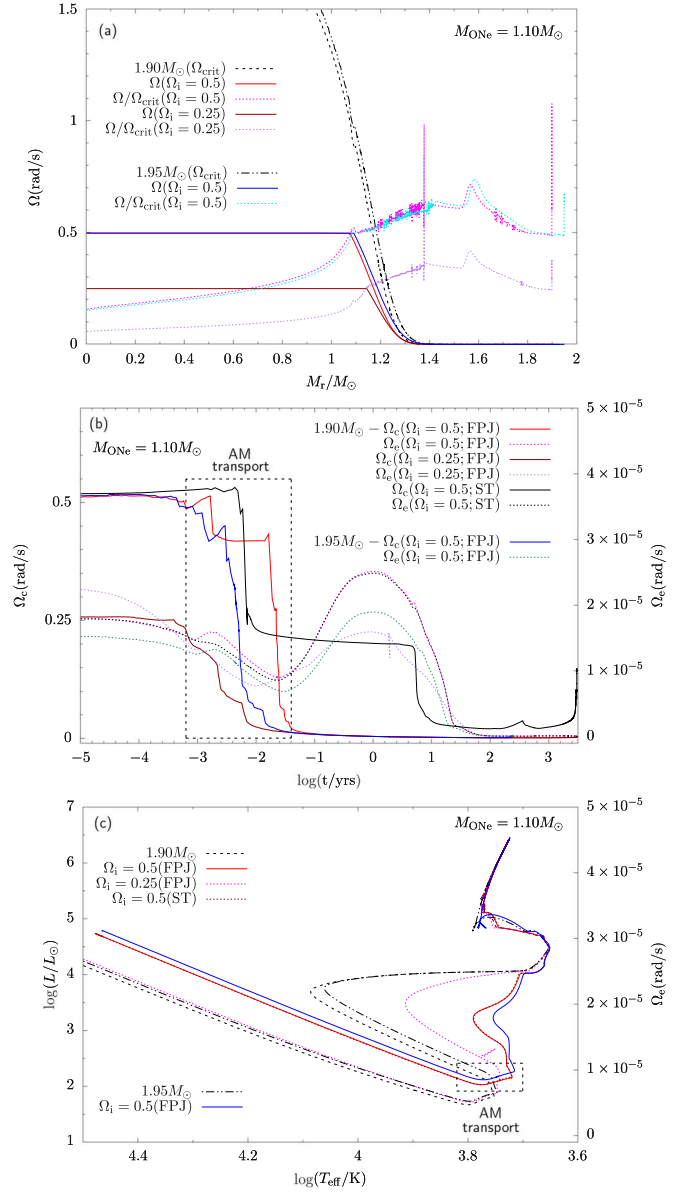


**Figure 9.** Evolutionary tracks when considering the rotational effect. Panel (a): initial rotation profile of 1.90 and 1.95  $M_{\odot}$  merger remnants. Solid, double dotted-dashed, and dotted lines represent the angular velocity, critical angular velocity, and ratio of angular and critical angular velocity of 1.90 and 1.95  $M_{\odot}$  merger remnants with different initial rotational velocities, respectively. Panel (b): evolution of the core (solid lines) and envelope (dotted lines) angular velocity of four models under different angular momentum transport prescriptions. The region inside the rectangle represents the most visible portion of the angular momentum transfer process. Panel (c): evolutionary tracks of four models compared with nonrotational models on the HRD. Similar to panel (b), the region inside the rectangle represents the most visible portion of the angular momentum transfer process.

angular velocity of the ONe core ( $\Omega_c = 0.5 \text{ rad s}^{-1}$ ) and a different rotational velocity in the envelope ( $\Omega_e = 0.5 \Omega_{\text{crit}}$ ), whereas the slow rotational models have the same angular velocity distributions but with  $\Omega_c = 0.25 \text{ rad s}^{-1}$  and  $\Omega_e = 0.25 \Omega_{\text{crit}}$ , respectively. Note that magnetic fields are quite effective in transporting angular momentum in double WD merger remnants; therefore, we adopt the angular momentum transport prescriptions described in Spruit (2002, hereafter ST02) and Fuller et al. (2019, hereafter FPJ19) to simulate the

**Table 1**

Major Parameters (Temperature, Luminosity, Mass-loss Rate, Stellar Mass, Stellar Radius, Stellar Age, and Final Fate) of J005311 from the Observations (Column (2)) and Our Theoretical Models When the Remnants Evolve to the Same Temperature as J005311 (Columns (3)–(6))

Parameter (1)	Observation J005311 (2)	ONe+CO WD		CO+CO WD	
		1.08+0.52 (3)	1.10+0.70 (4)	0.85+0.75 (5)	0.95+0.85 (6)
$T$ (K)	$211,000^{+40,000}_{-23,000}$	18,800–25,100	18,800–25,100	18,800–25,100	18,800–25,100
$L$ ( $L_{\odot}$ )	$39,810^{+20,144}_{-10,970}$	58,606–59,503	76,357–77,520	11,000–14,190	16,200–22,527
$\dot{M}$ ( $M_{\odot} \text{ yr}^{-1}$ )	$3.5(\pm 0.6) \times 10^{-6}$	$3.2\text{--}6.06 \times 10^{-6}$	$8.627\text{--}1.47 \times 10^{-6}$	$3.2\text{--}7.65 \times 10^{-9}$	$1.23\text{--}3.0 \times 10^{-8}$
$M$ ( $M_{\odot}$ )	$1.2 \pm 0.2$	1.186	1.252	1.313	1.463
$R$ ( $R_{\odot}$ )	$0.15 \pm 0.04$	0.128–0.23	0.148–0.26	0.06–0.108	0.08–0.122
Age (yr)	Unknown	1586–1644	1058–1082	11,371–18,072	12,339–15,863
Final fate	Unknown	ONe WD	ONe WD	ONe WD	Fe-CCSN

evolution of the remnants. Detailed physical inputs are given in the [Appendix](#).

From Figure 9, we can see that the remnants computed with the [FPJ19](#) prescription can transport angular momentum from the core to the envelope more rapidly. Thus, in this case, the envelope reaches the same angular velocity as the core within hours after merger. As the remnants expand toward the giant phase, the angular velocity of the envelope obviously decreases. The opacity of the outer shell changes due to the variation of temperature and rotational mixing process, which leads to differences in the phase in which luminosity increases. Although the final fate of the rotational models is same as that of the fiducial models, the difference in the core rotational velocity caused by the different prescriptions of angular momentum transport implies that the efficiency of angular momentum transport is one of the most important mechanisms influencing the rotational velocity of massive WDs.

## 5. J005311

Owing to the small quantity of massive double WD systems (e.g., [Liu & Wang 2020](#)) and the extremely short evolutionary time of the corresponding merger remnants (e.g., [Schwab 2021](#)), it is very difficult to observe such remnants. Fortunately, [Gvaramadze et al. \(2019\)](#) discovered a hot star in the constellation Cassiopeia (J005311; R.A. =  $00^{\text{h}}53^{\text{m}}11^{\text{s}}.21$ , decl. =  $+67^{\circ}30'21''$ ), located at the center of a circular mid-infrared nebula, by using data from the Wide-field Infrared Survey Explorer. The center star has a V-band magnitude of 15.5 mag and, according to Gaia DR2, is located at a distance of 3.06 kpc. The nebula appears as a circular shell and diffuse halo with linear radii of about 1.1 and 1.6 pc, respectively. The optical follow-up spectroscopy of J005311 obtained from the Russian 6 m telescope revealed an emission line-dominated spectrum similar to that of an oxygen-rich Wolf-Rayet (WO type) star. This emission line-dominated spectrum was later confirmed by [Garnavich et al. \(2020\)](#), who used the Large Binocular Telescope to obtain the spectra of J005311 and found significant variability in the profile of a strong O VI emission feature that was predicted to be caused by rapidly shifting subpeaks generated by clumpiness in the stellar wind of J005311. By employing the Potsdam Wolf-Rayet code, [Gvaramadze et al. \(2019\)](#) analyzed the optical spectrum of J005311 and found that the composition of the material at the base of the wind was dominated by oxygen and carbon with mass fractions of  $0.8 \pm 0.1$  and  $0.2 \pm 0.1$ , respectively. Based on the width and strength of the O VI emission line, they estimated that the wind mass-loss rate of the object was

$\dot{M} = (3.5 \pm 0.6) \times 10^{-6} M_{\odot} \text{ yr}^{-1}$  with a terminal wind velocity of  $v_{\infty} = 16,000 \pm 1000 \text{ km s}^{-1}$ . On the basis of these observations and the numerical results from [Schwab et al. \(2016\)](#), [Gvaramadze et al. \(2019\)](#) argued that J005311 was the outcome of a super-Chandrasekhar-mass double CO WD merger. Furthermore, they suggested that it would end its life as an Fe-CCSN.

[Oskinova et al. \(2020\)](#) reported on the first deep X-ray observation of J005311 and the first spectroscopic investigation of its nebula. They found that the central star is more luminous in the X-ray than single massive OB and WR stars. Combining with optical data, they claimed that J005311 is a super-Chandrasekhar-mass ONe+CO WD merger remnant. Similar to [Gvaramadze et al. \(2019\)](#), they suggested that J005311 would likely terminate its evolution as a Type I supernova, in which the final core collapse to an NS might be induced by an electron-capture process.

[Ritter et al. \(2021\)](#) later suggested that J005311 and its nebula are the residual core and ejecta of the 1181 AD explosion. They argued that this source is the result of an ONe+CO WD merger, and it is the only second Type Ia supernova living in our galaxy, which provided strong observational support for the double-degenerate merger scenario for Type Ia supernovae. [Lykou et al. \(2023\)](#) modeled the stellar remnant of J005311 and derived a magnetic field with an upper limit of 2.5 MG, and the luminosity indicated a remnant mass of  $1.2 \pm 0.2 M_{\odot}$  with an ejecta mass of  $0.15 \pm 0.05 M_{\odot}$ . Combined with the low mass ratio of Ne and O ( $\text{Ne/O} < 0.15$ ), they suggested that the object originated from the merger of double CO or CO+He WDs, arguing against the ONe WD merger origin of this object.

The origin of J005311 still remains uncertain. To understand the nature of J005311, we recalculated the ONe+CO WD merger models by considering the wind mass-loss and rotation process, since on one hand, the observation supported that the object has an extremely strong mass-loss process, and on the other hand, double WD merger remnants could keep a portion of the orbital angular momentum. As in the prescription described in Section 4.5, we inject torque into 1.6 and 1.8  $M_{\odot}$  merger remnants to change their initial rotational profiles until their core ( $\Omega_{\text{c}}$ ) and envelope ( $\Omega_{\text{e}}$ ) rotational velocity reached  $\Omega_{\text{c}} = 0.5 \text{ rad s}^{-1}$  and  $\Omega_{\text{e}} = 0.5 \Omega_{\text{crit}}$  ( $\Omega_{\text{crit}}$  is the Keplerian velocity for each mass zone). The corresponding rotational profile can approximately describe the properties of the merger remnants with a similar total mass (e.g., [Lorén-Aguilar et al. 2009](#)). During the postmerger evolution, we simply consider [Bloeker's](#) wind mass-loss prescription (e.g., [Bloeker 1995](#)) with a typical scaling factor of  $\eta_{\text{B}} = 0.05$  to produce a strong

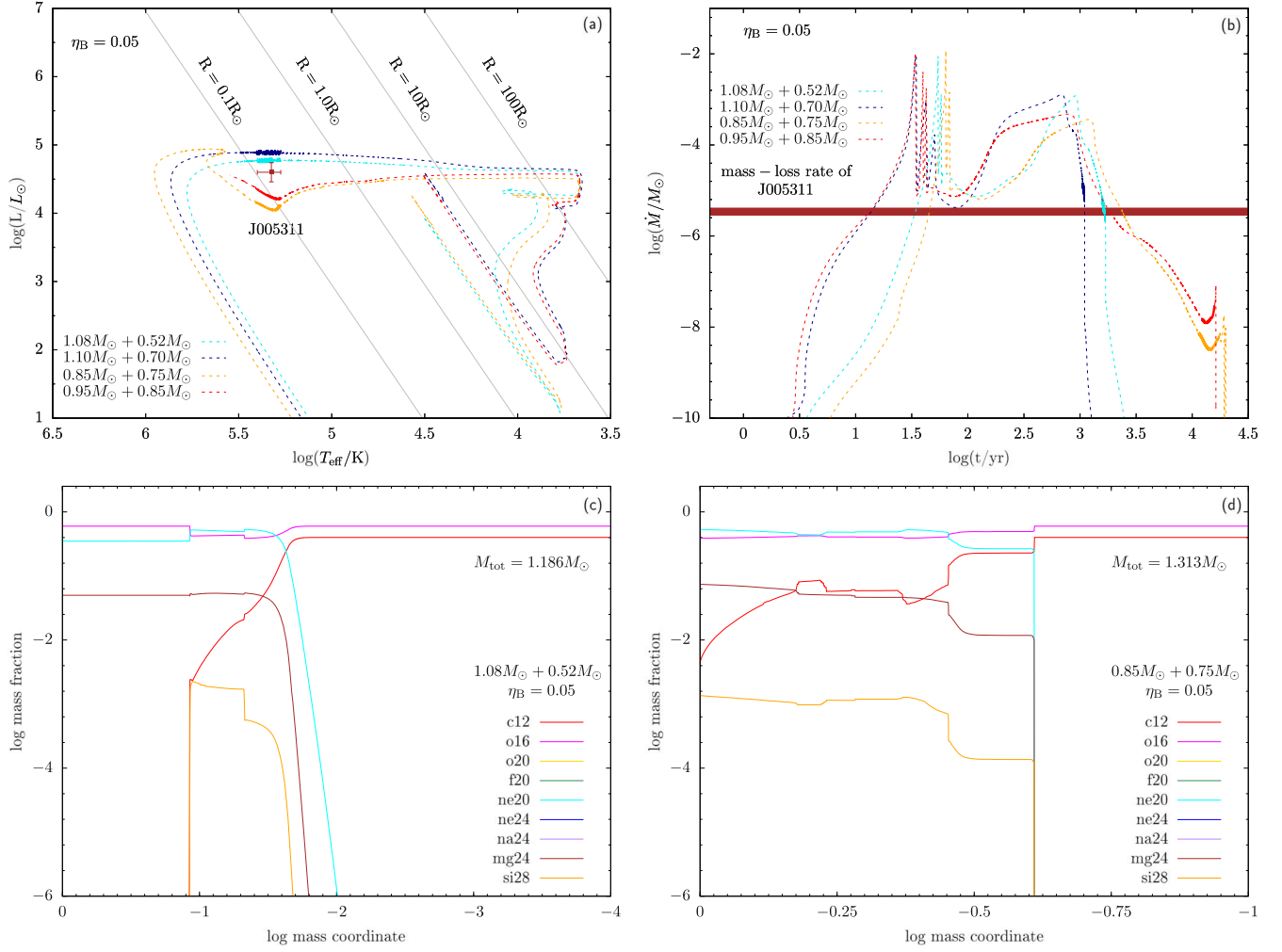


**Figure 10.** Evolution of ONE+CO and CO+CO WD models when considering rotation ( $\Omega_c = 0.5 \text{ rad s}^{-1}$ ,  $\Omega_e = 0.5 \Omega_{\text{crit}}$ ) and Bloeker’s wind mass-loss prescription ( $\eta_B = 0.05$ ). Panel (a): HRD. Cyan and navy lines represent the evolution of ONE+CO WD merger remnants with total masses equal to  $1.60$  and  $1.80 M_\odot$ , respectively. In comparison, the evolution of double CO WD mergers with the same total masses (a mass ratio equal to  $0.9$ ) are shown as orange and red lines, respectively. Panel (b): evolution of wind mass-loss rate for the corresponding models. The brown point with an error bar in panel (a) represents the position of J005311 on the HRD, whereas the brown shaded area in panel (b) represents the estimated wind mass-loss rate of J005311. The thick solid portion of each line in panels (a) and (b) represents the position of each model when it evolves to the same temperature as J005311. Panels (c) and (d): elemental abundance distributions of ONE+CO and CO+CO WD models at the moment when they evolve to the position close to J005311 on the HRD, respectively.

mass-loss process. In comparison, we also calculated CO+CO WD merger models under the same physical inputs.

Some key stellar parameters of J005311 and our models are listed in Table 1. Figure 10 shows that the evolutionary tracks on the HRD of all four models pass through a position close to J005311. However, the double CO WD merger model has very low mass-loss rates, in the range from  $10^{-9}$  to a few  $10^{-8} M_\odot \text{ yr}^{-1}$ , when the corresponding remnant has a temperature similar to that of J005311. The reason is that such a merger remnant experiences off-center carbon burning through flashes, which prevents stationary shell burning near the edge of the degenerate core, resulting in a lower-luminosity remnant. For the ONE+CO WD model, because of the initially low mass and the short evolutionary time of the remnant due to the strong wind mass-loss process, off-center neon burning cannot be triggered after the merger. Thus, the remnant still maintains shell carbon burning and has relatively high mass-loss rates comparable to the values inferred from observations.

Besides, results from double CO and ONE+CO mergers allow one to infer different model remnant masses when the associated tracks reach the position of J005311 in the HRD.

After experiencing extremely strong stellar wind, the masses of ONE+CO WD merger remnants decrease and reach values in the range from  $1.186$  to  $1.253 M_\odot$ . These sub-Chandrasekhar remnant mass values are consistent with those derived from observation, i.e.,  $1.2 \pm 0.2 M_\odot$  (e.g., Lykou et al. 2023). For the double CO WD merger counterparts, the initially massive remnant ( $M^i = 1.80 M_\odot$ ) is still super-Chandrasekhar mass ( $1.473 M_\odot$ ), which predicts a different evolutionary outcome for J005311; i.e., it will undergo a supernova explosion through an Fe-CCSN. The final fate of the less massive double CO merger remnant ( $M^i = 1.60 M_\odot$ ) is the same as that of the ONE+CO WD merger of the same initial mass. However, the radius of the former is too small to explain the observed properties of J005311. Note that for the super-Chandrasekhar-mass remnants, the deflagration of oxygen may produce an ONeFe WD with mass close to  $1.2 M_\odot$  (e.g., Jones et al. 2016b), which may also show similar characteristics to J005311. However, such a postexplosion remnant should have an extremely low carbon abundance (e.g., Jones et al. 2019), which may not be consistent with J005311. Hence, we suggest that J005311 derives from an ONE+CO WD merger, and, in the future, it is

expected to evolve to an ONe WD with a mass close to  $1.20 M_{\odot}$  (see also Kashiyama et al. 2019).

Lykou et al. (2023) argued that J005311 originates from a double CO WD merger rather than an ONe+CO WD merger, since the ejecta of J005311 is deficient in neon. Based on our simulations, the convective regions in the envelope of neither the ONe+CO nor the double CO WD remnants are able to penetrate the carbon-burning zone. This leads one to expect neon-deficient ejecta at the corresponding evolutionary stage of J005311 (see panels (c) and (d) of Figure 10). Note that, owing to the occurrence of a mixing process during the double WD merger, the base of the CO envelope in the ONe+CO merger remnant could show neon enhancement. However, according to Dan et al. (2014), the abundance of neon at the base of the CO envelope cannot be higher than 20%, which may still be consistent with a low mass ratio of Ne and O as the remnant evolves to a pre-WD.

Meanwhile, the nebula of J005311 is 1.1–1.6 pc from the central star. Ritter et al. (2021) argued that the nebula stemmed from the supernova explosion of 1181 AD. If an NS is formed after the supernova explosion, it is difficult to explain why the central remnant remains at a constant luminosity within 100 yr (e.g., Oskinova et al. 2020). Considering that the wind velocity of the pre-WD is on the order of magnitude of  $1000 \text{ km s}^{-1}$ , it will take 1120–1600 yr to reach the size of the nebula of J005311, which is consistent with the evolutionary time of the ONe+CO WD merger remnant. Therefore, we suggest that J005311 may have resulted from an ONe+CO WD merger, and its nebula may have formed through the strong wind-loss process during its evolution. In addition, we predict that this object will form a massive WD rather than undergo a supernova explosion thousand of years later.

## 6. Summary

In this work, we investigated the evolution of ONe+CO WD merger remnants for the first time. We found that the evolutionary outcomes of such merger remnants are related to their initial masses; i.e., less massive remnants ( $M \leq 1.90 M_{\odot}$ ) would experience a shell carbon-burning phase to increase the core mass before off-center neon burning, whereas more

massive remnants ( $M \geq 1.95 M_{\odot}$ ) would trigger off-center neon burning soon after the merger. By considering wind mass-loss prescriptions, the less massive remnants are more sensitive to the wind mass-loss rate, meaning that their final fates may be as ONe WDs or NSs. By contrast, the more massive remnants may always experience supernova explosions to form ONeFe WDs. Using the mass-loss prescription by Bloeker (1995), our models can explain the observational properties of J005311, including temperature, luminosity, wind mass-loss rate, formation of a nebula, evolutionary time, and abundance of the ejecta. From this, we can derive that our study may be able to provide some constraints on the wind mass-loss rates of H-/He-deficient giant-like objects similar to J005311. For example, due to the relevance of dust in both environments, their wind mass-loss process could present analogies with that occurring in AGB stars. Finally, we strongly suggest that J005311 originated from the merger of an ONe WD and a CO WD, and the final fate of this object will be to become a massive ONe WD rather than a supernova explosion.

We thank Matthias Kruckow, Xiangcun Meng, Zhengwei Liu, Jiangdan Li, Hailiang Chen, and Dongdong Liu for helpful discussion. This study is supported by the National Key R&D Program of China (No. 2021YFA1600404), the National Natural Science Foundation of China (NSFC grants 12003013, 12225304, 12288102, and 12033003), the Western Light Project of CAS (No. XBZG-ZDSYS-202117), the science research grants from the China Manned Space Project (No. CMS-CSST-2021-A12), the Yunnan Fundamental Research Projects (No. 202001AS070029), the Scholar Program of the Beijing Academy of Science and Technology (DZ: BS202002), and the Tencent Xplorer Prize.

## Appendix

In Tables 2–8, we list all of the models in our calculations that are partly mentioned in Sections 3–5. The source files for our MESA models are publicly available on Zenodo at doi:10.5281/zenodo.7456455.

**Table 2**  
Models Involved in Section 3.2

Model (1)	$M_{\text{tot}} (M_{\odot})$ (2)	$\ln(s_{\text{env}}/\text{erg g}^{-1} \text{K}^{-1})$ (3)	$T_{\text{max}}/10^8 \text{ K}$ (4)	Stopping Condition (5)	$t \text{ yr}^{-1}$ (6)	Expected Fate (7)
ONe+CO						
1.10 + 0.65	1.75	8.875	10.484	$\log(T_c/\text{K}) > 9.34$	9687	NS
1.10 + 0.70	1.80	8.890	10.788	$\log(T_c/\text{K}) > 9.34$	8173	NS
1.15 + 0.65	1.80	8.890	11.660	$\log(T_c/\text{K}) > 9.34$	5681	NS
1.10 + 0.75	1.85	8.905	11.138		6202	NS
1.15 + 0.70	1.85	8.905	11.929	$\log(T_c/\text{K}) > 9.34$	4112	NS
1.20 + 0.65	1.85	8.905	13.114		994	NS
1.10 + 0.80	1.90	8.920	11.579		3125	NS
1.15 + 0.75	1.90	8.920	12.339	$\log(T_c/\text{K}) > 9.34$	1729	NS
1.20 + 0.70	1.90	8.920	13.398		178	ONeFe WD
1.10 + 0.85	1.95	8.935	12.154		240	ONeFe WD
1.15 + 0.80	1.95	8.935	12.782	$\log(T_c/\text{K}) > 9.34$	179	ONeFe WD
1.20 + 0.75	1.95	8.935	13.824		107	ONeFe WD
1.10 + 0.90	2.00	8.950	12.649		134	ONeFe WD
1.15 + 0.85	2.00	8.950	13.242	$\log(T_c/\text{K}) > 9.34$	163	ONeFe WD
1.20 + 0.80	2.00	8.950	14.271		47	ONeFe WD
1.10 + 0.95	2.05	8.965	13.330		106	ONeFe WD
1.15 + 0.90	2.05	8.965	13.850	$\log(T_c/\text{K}) > 9.34$	66	ONeFe WD
1.20 + 0.85	2.05	8.965	14.771		39	ONeFe WD
1.10 + 1.00	2.10	8.980	14.053		59	ONeFe WD
1.15 + 0.95	2.10	8.980	14.556	$\log(T_c/\text{K}) > 9.34$	43	ONeFe WD
1.20 + 0.90	2.10	8.980	15.387		25	ONeFe WD
1.10 + 1.05	2.15	8.995	14.959		...	ONeFe WD
1.15 + 1.00	2.15	8.995	15.486	$\log(T_c/\text{K}) > 9.34$	51	ONeFe WD
1.20 + 0.95	2.15	8.995	16.234		20	ONeFe WD
1.15 + 1.05	2.20	9.010	16.441	$\log(T_c/\text{K}) > 9.34$	232	ONeFe WD
1.20 + 1.00	2.20	9.010	10.720	$\log(T_c/\text{K}) > 9.34$	14	ONeFe WD
1.20 + 1.05	2.25	9.025	18.350	$\log(T_c/\text{K}) > 9.34$	8.4	ONeFe WD

**Note.** The columns are as follows. (1) Masses of ONe and CO WDs. (2) Total mass of merger remnant. (3) Natural logarithm of envelope entropy of remnant. (4) Maximum temperature of remnant. (5) Stage at which calculation is stopped. (6) Evolution times from the beginning of our calculations to the stopping conditions (the model of 1.10 + 1.05 meets some numerical problems during its evolution). (7) Final evolutionary outcome of the remnant, where NS represents that the remnant experiences an ECSN to form an NS, and ONeFe WD represents that the remnant experiences an ECSN to form an ONeFe WD.

**Table 3**  
Models Involved in Section 4.1

Model (1)	$M_{\text{tot}} (M_{\odot})$ (2)	$\ln(s_{\text{env}}/\text{erg g}^{-1} \text{K}^{-1})$ (3)	$T_{\text{max}}/10^8 \text{ K}$ (4)	Stopping Condition (5)	$t \text{ yr}^{-1}$ (6)	Expected Fate (7)
ONe+CO						
1.10 + 0.80	1.90	8.70	15.133	$\log(T_c/\text{K}) > 9.34$	80	ONeFe WD
1.10 + 0.80	1.90	9.10	9.773	$\log(T_c/\text{K}) > 9.34$	10,963	NS
1.10 + 0.85	1.95	8.70	17.034	$\log(T_c/\text{K}) > 9.34$	45.5	ONeFe WD
1.10 + 0.85	1.95	9.10	10.228	$\log(T_c/\text{K}) > 9.34$	8788	NS

**Note.** The columns are as follows. (1) Masses of ONe and CO WDs. (2) Total mass of merger remnant. (3) Natural logarithm of envelope entropy of remnant. (4) Maximum temperature of remnant. (5) Stage at which calculation is stopped. (6) Evolution times from the beginning of our calculations to the stopping conditions. (7) Final evolutionary outcome of the remnant.

**Table 4**  
Models Involved in Section 4.2

Model (1)	$M_{\text{tot}} (M_{\odot})$ (2)	Mass-loss Prescription (3)	Stopping Condition (4)	$t \text{ yr}^{-1}$ (5)	Expected Fate (6)
ONe+CO					
1.10 + 0.80	1.90	Reimers ( $\eta_{\text{R}} = 0.5$ )	$\log(T_{\text{c}}/K) > 9.34$	3121	NS
1.10 + 0.80	1.90	Bloecker ( $\eta_{\text{B}} = 0.05$ )	$\log(L/L_{\odot}) < 1.0$	29,960	ONe WD
1.10 + 0.85	1.95	Reimers ( $\eta_{\text{R}} = 0.5$ )	$\log(T_{\text{c}}/K) > 9.34$	242	ONeFe WD
1.10 + 0.85	1.95	Bloecker ( $\eta_{\text{B}} = 0.05$ )	$\log(T_{\text{c}}/K) > 9.34$	241	ONeFe WD

**Note.** The columns are as follows. (1) Masses of ONe and CO WDs. (2) Total mass of merger remnant. (3) Wind mass-loss prescription considered in the corresponding model, where Reimers ( $\eta_{\text{R}} = 0.5$ ) represents models that adopt Reimers' wind mass-loss prescription (Reimers 1975) with a factor of  $\eta_{\text{R}} = 0.5$ , and Bloecker ( $\eta_{\text{B}} = 0.05$ ) represents models that adopt Bloecker's wind mass-loss prescription (Bloecker 1995) with a factor of  $\eta_{\text{B}} = 0.05$ . (4) Stage at which calculation is stopped. (5) Evolution times from the beginning of our calculations to the stopping conditions. (6) Final evolutionary outcome of the remnant, where NS represents that the remnant experiences an ECSN to form an NS, and ONeFe WD represents that the remnant experiences an ECSN to form an ONeFe WD.

**Table 5**  
Models Involved in Section 4.3

Model (1)	$M_{\text{tot}} (M_{\odot})$ (2)	$f_{\text{He}}$ in Envelope (3)	Stopping Condition (4)	$t \text{ yr}^{-1}$ (5)	Expected Fate (6)
ONe+CO					
1.10 + 0.50	1.60	0%	$\log(T_{\text{c}}/K) > 9.34$	12,507	NS
ONe+HeCO					
1.10 + 0.50	1.60	20%	$\log(T_{\text{c}}/K) > 9.34$	27,859	NS

**Note.** The columns are as follows. (1) Masses of ONe and CO WDs. (2) Total mass of merger remnant. (3) Mass fraction of  $^4\text{He}$  in CO envelope. (4) Stage at which calculation is stopped. (5) Evolution times from the beginning of our calculations to the stopping conditions. (6) Final evolutionary outcome of the remnant, where NS represents that the remnant experiences an ECSN to form an NS.

**Table 6**  
Models Involved in Section 4.4

Model (1)	$M_{\text{tot}} (M_{\odot})$ (2)	$f_{^{16}\text{O}}$ (3)	$f_{^{20}\text{Ne}}$ (4)	$f_{^{24}\text{Mg}}$ (5)	$f_{^{23}\text{Na}}$ (6)	$f_{^{25}\text{Mg}}$ (7)	Stopping Condition (8)	$t \text{ yr}^{-1}$ (9)	Expected Fate (10)
ONe+CO									
1.10 + 0.80	1.90	60%	35%	5%	0%	0%	$\log(T_{\text{c}}/K) > 9.34$	3125	NS
1.10 + 0.80	1.90	54%	35%	5%	5%	1%	$\log(T_{\text{c}}/K) > 9.34$	1937	NS
1.10 + 0.85	1.95	60%	35%	5%	0%	0%	$\log(T_{\text{c}}/K) > 9.34$	240	ONeFe WD
1.10 + 0.85	1.95	54%	35%	5%	5%	1%	$\log(T_{\text{c}}/K) > 9.34$	197	ONeFe WD

**Note.** The columns are as follows. (1) Masses of ONe and CO WDs. (2) Total mass of merger remnant. (3) Mass fraction of  $^{16}\text{O}$  in ONe core. (4) Mass fraction of  $^{20}\text{Ne}$  in ONe core. (5) Mass fraction of  $^{24}\text{Mg}$  in ONe core. (6) Mass fraction of  $^{23}\text{Na}$  in ONe core. (7) Mass fraction of  $^{25}\text{Mg}$  in ONe core. (8) Stage at which calculation is stopped. (9) Evolution times from the beginning of our calculations to the stopping conditions. (10) Final evolutionary outcome of the remnant, where NS represents that the remnant experiences an ECSN to form an NS, whereas ONeFe WD represents that the remnant experiences an ECSN to form an ONeFe WD.

**Table 7**  
Models Involved in Section 4.5

Model (1)	$M_{\text{tot}} (M_{\odot})$ (2)	$\Omega_c$ (rad s $^{-1}$ ) (3)	$\Omega_c (\Omega_{\text{crit}})$ (4)	AM Transport (5)	Stopping Condition (6)	$t$ yr $^{-1}$ (7)	Expected Fate (8)
ONe+CO							
1.10 + 0.80	1.90	0.50	0.50	FPJ19	$\log(T_c/K) > 9.34$	3020	NS
1.10 + 0.80	1.90	0.50	0.50	ST02	$\log(T_c/K) > 9.34$	3050	NS
1.10 + 0.80	1.90	0.25	0.25	FPJ19	$\log(T_c/K) > 9.34$	3127	NS
1.10 + 0.80	1.90	0.25	0.25	ST02	$\log(T_c/K) > 9.34$	3135	NS
1.10 + 0.85	1.95	0.50	0.50	FPJ19	$\log(T_c/K) > 9.34$	243	ONeFe WD
1.10 + 0.85	1.95	0.50	0.50	ST02	$\log(T_c/K) > 9.34$	214	ONeFe WD
1.10 + 0.85	1.95	0.25	0.25	FPJ19	$\log(T_c/K) > 9.34$	243	ONeFe WD
1.10 + 0.85	1.95	0.25	0.25	ST02	$\log(T_c/K) > 9.34$	245	ONeFe WD

**Note.** The columns are as follows. (1) Masses of ONe and CO WDs. (2) Total mass of merger remnant. (3) Rotation velocity of core in radians per second. (4) Rotation velocity of each mass zone in the envelope divided by Keplerian velocity of the corresponding mass zone. (5) Angular momentum transport prescription adopted in the corresponding model. (6) Stage at which calculation is stopped. (7) Evolution times from the beginning of our calculations to the stopping conditions. (8) Final evolutionary outcome of the remnant, where NS represents that the remnant experiences an ECSN to form an NS, and ONeFe WD represents that the remnant experiences an ECSN to form an ONeFe WD.

**Table 8**  
Models Involved in Section 5

Model (1)	$M_{\text{tot}} (M_{\odot})$ (2)	$\Omega_c$ (rad s $^{-1}$ ) (3)	$\Omega_c (\Omega_{\text{crit}})$ (4)	AM Transport (5)	Mass-loss Prescription (6)	Stopping Condition (7)	$t$ yr $^{-1}$ (8)	Expected Fate (9)
ONe+CO								
1.08 + 0.52	1.60	0.50	0.50	FPJ19	Bloeker ( $\eta_B = 0.05$ )	$\log(L/L_{\odot}) < 1.0$	86,306	ONe WD
1.10 + 0.70	1.80	0.50	0.50	FPJ19	Bloeker ( $\eta_B = 0.05$ )	$\log(L/L_{\odot}) < 1.0$	56,030	ONe WD
CO+CO								
0.85 + 0.75	1.60	0.50	0.50	FPJ19	Bloeker ( $\eta_B = 0.05$ )	$\log(L/L_{\odot}) < 1.0$	52,378	ONe WD
0.95 + 0.85	1.80	0.50	0.50	FPJ19	Bloeker ( $\eta_B = 0.05$ )	Ne ignition	16,276	Fe-CCSN

**Note.** The columns are as follows. (1) Masses of ONe and CO WDs. (2) Total mass of merger remnant. (3) Rotation velocity of core in radians per second. (4) Rotation velocity of each mass zone in the envelope divided by Keplerian velocity of the corresponding mass zone. (5) Angular momentum transport prescription adopted in the corresponding model. (6) Wind mass-loss prescription considered in the corresponding model, where Reimers ( $\eta_R = 0.5$ ) represents models that adopt Reimers' wind mass-loss prescription (Reimers 1975) with a factor of  $\eta_R = 0.5$ , and Bloeker ( $\eta_B = 0.05$ ) represents models that adopt Bloeker's wind mass-loss prescription (Bloeker 1995) with a factor of  $\eta_B = 0.05$ . (7) Stage at which calculation is stopped. (8) Evolution times from the beginning of our calculations to the stopping conditions. (9) Final evolutionary outcome of the remnant, where ONe WD represents that the remnant ends its evolution as an ONe WD, and Fe-CCSN represents that the remnant experiences an Fe-CCSN to form an NS.

## ORCID iDs

Chengyuan Wu  <https://orcid.org/0000-0002-2452-551X>

Jie Lin  <https://orcid.org/0000-0003-3965-6931>

Xiaofeng Wang  <https://orcid.org/0000-0002-7334-2357>

Zhanwen Han  <https://orcid.org/0000-0001-9204-7778>

Bo Wang  <https://orcid.org/0000-0002-3231-1167>

## References

- Bloeker, T. 1995, *A&A*, 297, 727
- Brooks, J., Schwab, J., Bildsten, L., et al. 2017, *ApJ*, 850, 127
- Chugunov, A. I., Dewitt, H. E., & Yakovlev, D. G. 2007, *PhRvD*, 76, 025028
- Dan, M., Rosswog, S., Brüggen, M., & Podsiadlowski, P. 2014, *MNRAS*, 438, 14
- Denissenkov, P. A., Herwig, F., Truran, J. W., & Paxton, B. 2013, *ApJ*, 772, 37
- Doherty, C. L., Gil-Pons, P., Siess, L., & Lattanzio, J. C. 2017, *PASA*, 34, e056
- Eldridge, J. J., & Tout, C. A. 2004, *MNRAS*, 353, 87
- Farmer, R., Fields, C. E., & Timmes, F. X. 2015, *ApJ*, 807, 184
- Fuller, J., Piro, A. L., & Jermyn, A. S. 2019, *MNRAS*, 485, 3661
- Garnavich, P., Littlefield, C., Pogge, R., & Wood, C. 2020, *RNAAS*, 4, 167
- Gvaramadze, V. V., Gräfener, G., Langer, N., et al. 2019, *Natur*, 569, 684
- Holberg, J. B. 2009, *JPhCS*, 172, 012022
- Ibeling, D., & Heger, A. 2013, *ApJL*, 765, L43
- Iglesias, C. A., & Rogers, F. J. 1996, *ApJ*, 464, 943
- Itoh, N., Hayashi, H., Nishikawa, A., & Kohyama, Y. 1996, *ApJS*, 102, 411
- Jeffery, C. S. 1988, *MNRAS*, 235, 1287
- Jones, S., Hirschi, R., & Nomoto, K. 2014, *ApJ*, 797, 83
- Jones, S., Ritter, C., Herwig, F., et al. 2016a, *MNRAS*, 455, 3848
- Jones, S., Röpkke, F. K., Fryer, C., et al. 2019, *A&A*, 622, A74
- Jones, S., Röpkke, F. K., Pakmor, R., et al. 2016b, *A&A*, 593, A72
- Kashiyama, K., Fujisawa, K., & Shigezuma, T. 2019, *ApJ*, 887, 39
- Kashyap, R., Haque, T., Lorén-Aguilar, P., García-Berro, E., & Fisher, R. 2018, *ApJ*, 869, 140
- Kitaura, F. S., Janka, H. T., & Hillebrandt, W. 2006, *A&A*, 450, 345
- Liu, D., & Wang, B. 2020, *MNRAS*, 494, 3422
- Lorén-Aguilar, P., Isern, J., & García-Berro, E. 2009, *A&A*, 500, 1193
- Lykou, F., Parker, Q. A., Ritter, A., et al. 2023, *ApJ*, 944, 120
- Napiwotzki, R. 2009, *JPhCS*, 172, 012004
- Nelemans, G., Yungelson, L. R., Portegies Zwart, S. F., & Verbunt, F. 2001, *A&A*, 365, 491

- Nomoto, K., & Kondo, Y. 1991, [ApJL](#), **367**, L19
- Oskinova, L. M., Gvaramadze, V. V., Gräfener, G., Langer, N., & Todt, H. 2020, [A&A](#), **644**, L8
- Paxton, B., Bildsten, L., Dotter, A., et al. 2011, [ApJS](#), **192**, 3
- Paxton, B., Cantiello, M., Arras, P., et al. 2013, [ApJS](#), **208**, 4
- Paxton, B., Marchant, P., Schwab, J., et al. 2015, [ApJS](#), **220**, 15
- Paxton, B., Schwab, J., Bauer, E. B., et al. 2018, [ApJS](#), **234**, 34
- Paxton, B., Smolec, R., Schwab, J., et al. 2019, [ApJS](#), **243**, 10
- Poelarends, A. J. T. 2007, PhD thesis, Univ. Utrecht, Netherlands
- Reimers, D. 1975, [MSRSL](#), **8**, 369
- Ritossa, C., García-Berro, E., & Iben, I. J. 1999, [ApJ](#), **515**, 381
- Ritter, A., Parker, Q. A., Lykou, F., et al. 2021, [ApJL](#), **918**, L33
- Schwab, J. 2019, [ApJ](#), **885**, 27
- Schwab, J. 2021, [ApJ](#), **906**, 53
- Schwab, J., Bildsten, L., & Quataert, E. 2017, [MNRAS](#), **472**, 3390
- Schwab, J., Quataert, E., & Bildsten, L. 2015, [MNRAS](#), **453**, 1910
- Schwab, J., Quataert, E., & Kasen, D. 2016, [MNRAS](#), **463**, 3461
- Siess, L. 2007, [A&A](#), **476**, 893
- Siess, L. 2010, [A&A](#), **512**, A10
- Spruit, H. C. 2002, [A&A](#), **381**, 923
- Wu, C., Wang, B., Wang, X., Maeda, K., & Mazzali, P. 2020, [MNRAS](#), **495**, 1445
- Wu, C., Xiong, H., & Wang, X. 2022, [MNRAS](#), **512**, 2972
- Zhang, X., Jeffery, C. S., Chen, X., & Han, Z. 2014, [MNRAS](#), **445**, 660